Waveguide Microactuators Self-Rolled Around an Optical Fiber Taper

Yang Zong, Minjie Xi, Yunqi Wang, Guohonghao Zeng, Dongliang Hu, Huihui Hu, Xiaoqi Hou, Kewang Nan, Xiangzhong Chen, Fan Xu, Oliver G. Schmidt, Yongfeng Mei, and Jizhai Cui*

Precisely capturing and manipulating microscale objects, such as individual cells and microorganisms, is fundamental to advancements in biomedical research and microrobotics. Photoactuators based on optical fibers serving as flexible, unobstructed waveguides are well-suited for these operations, particularly in confined locations where free-space illumination is impractical. However, integrating optical fibers with microscale actuators poses significant challenges due to size mismatch, resulting in slow responses inadequate for handling motile micro-objects. This study designs microactuators based on hydrogel/Au bilayer heterostructures that self-roll around a tapered optical fiber. This self-rolling mechanism enables the use of thin hydrogel layers only a few micrometers thick, which rapidly absorb and release water molecules during a phase transition. The resulting microactuators exhibit low bending stiffness and extremely fast responses, achieving large bending angles exceeding 800° within 0.55 s. Using this technique, this study successfully captures rapidly swimming Chlamydomonas and Paramecium, and demonstrates programmable non-reciprocal motion for effective non-contact manipulation of yeast cells. This approach provides a versatile platform for microscale manipulations and holds promise for advanced biomedical applications.

1. Introduction

Soft actuators have great potential for future applications such as soft grippers,[1,2] artificial muscles,[3,4] and biomimetic systems.[5,6] They can be driven by a variety of external stimuli such as light,[7,8] temperature,[9] magnetic fields,[10,11] electric fields[12] and humidity.[13] Among these control methods, light actuation is of particular interest, since light can be easily patterned both spatially and temporally and applied remotely with numerous control parameters including wavelength, polarization, and intensity.[14,15] Typical photoactuation adopts free-space illumination,[16,17] where an unblocked and clean optical path between the actuators and the light source is essential. This may result in undesirable attenuation due to light scattering and absorption during propagation, and refraction when passing through boundaries between different media, thus hindering its application in unstructured and

Y. Zong, M. Xi, Y. Wang, G. Zeng, Y. Mei, J. Cui
Department of Materials Science
Fudan University
Shanghai 200438, China
E-mail: jzcui@fudan.edu.cn

Y. Zong, M. Xi, Y. Wang, G. Zeng, X. Chen, O. G. Schmidt, Y. Mei, J. Cui
International Institute of Intelligent Nanorobots and Nanosystems
Fudan University
Shanghai 200438, China

D. Hu, X. Hou
School of Chemistry and Materials Science
Hangzhou Institute for Advanced Study
University of Chinese Academy of Sciences
Hangzhou 310024, China

D. Hu, X. Hou
University of Chinese Academy of Sciences
Beijing 100049, China

H. Hu, K. Nan
State Key Laboratory of Advanced Drug Delivery and Release Systems
College of Pharmaceutical Sciences
Zhejiang University
Hangzhou 310058, China

X. Chen, Y. Mei, J. Cui
Yiwu Research Institute of Fudan University
Yiwu, Zhejiang 322000, China

X. Chen, Y. Mei
Shanghai Frontiers Science Research Base of Intelligent Optoelectronics and Perception
Institute of Optoelectronics
Fudan University
Shanghai 200438, China

F. Xu
Institute of Mechanics and Computational Engineering
Department of Aeronautics and Astronautics
Fudan University
Shanghai 200433, China

O. G. Schmidt
Research Center for Materials
Architectures and Integration of Nanomembranes (MAIN)
Chemnitz University of Technology
09111 Chemnitz, Germany

confined working environments.[18,19] Optical fibers are flexible waveguides that provide unobstructed paths for light propagation over long distances with extremely low attenuation, avoiding issues such as scattering and refraction at media interfaces,[20] and have recently been implemented for photoactuation.[21,22,23,24] Photoactuators based on fiber optics therefore have the potential to operate in previously inaccessible locations, such as navigating through curved catheters for in vivo applications.

Despite extensive studies on both photoactuators and fiber-optic technologies, their proper integration remains challenging. Photoactuators that exhibit large deformation and fast response typically employ thin thickness, primarily because thinner structures have reduced thermal conduction times[25,26] and lower bending stiffness.[26,27] However, current integration methods often demand photoactuators with thicknesses of at least 30–700 µm[21,22,23,24]—comparable to or even greater than the diameter of the fiber tip (usually >100 µm)—thus inevitably compromising actuation speed and bending amplitude. For example, Zhou et al. face-to-face bonded a microactuator onto a fiber tip, achieving a bending angle ≈60° with a response time exceeding 50 s.[23] Zmyslony et al. employed in situ growth of microactuators on the fiber tip, achieving a bending angle ≈17° with a response time longer than 2 s.[24] Xiao et al. directly embedded an optical fiber taper within a poly-dimethylsiloxane/Au nanorod-graphene oxide photothermal film via casting in a 0.5 mm × 10 mm photoactuator.[22] Although this approach provided impressive performances with large bending angles (>270°) and fast response (1.8 s for 180°)—primarily due to the material used with increased optical coupling efficiency—the casting method remains primarily suitable for relatively large and thick photoactuators.

In this work, we propose a novel strategy for integrating thin film (≈2 µm thick) microactuators with optical fibers by self-rolling the microactuator onto the tip of the optical fiber taper. This approach effectively decouples the actuator's design from its integration with the fiber, allowing for a broader range of structural designs and the utilization of thinner actuators capable of large deformations and rapid responses. A thin and soft micrometer-scale hydrogel/Au bilayer heterostructure, which has previously demonstrated significant deformation and extremely short response times,[26] is adopted to enable self-rolling and secure attachment to the tip of an optical fiber taper (**Figure 1a**). A 1550 nm laser delivered through the fiber heats the hydrogel, inducing a phase change that results in substantial deformation. A micromanipulation stage with three translational (along x, y, and z axes) and one rotational (along the x-axis) degree of freedom provides dexterous deployment of the microactuator.

Analogous to a frog's tongue—a natural thin and soft muscle capable of rapid, extensive, and diverse deformations for predation—our 300 µm-long microactuator demonstrates a bending angle exceeding 800° in ≈0.55 s, transitioning from an almost flat, fully extended state to a rolled-up state with a diameter of ≈38.8 µm (Figure 1b; Movie S1, Supporting Information). Consequently, this microactuator can effectively capture and release fast-moving microorganisms (Figure 1c–f; Movies S2 and S3, Supporting Information). The spherical Chlamydomonas (Figure 1c) and sole-shaped Paramecium (Figure 1e) were observed swimming at maximum speeds of ≈110 and 600 µm s^{-1}, respectively. As depicted in Figure 1d, the microactua-

tor is fully extended when the laser is activated (t = 0 s). Upon the approach of the Chlamydomonas (t = 2.43 s), the laser is turned off, causing the microactuator to roll back and successfully capture the Chlamydomonas (t = 2.88 s), which is subsequently released (t = 12 s) by reactivating the laser to unfold the microactuator. We repeated the capture and release of Chlamydomonas 21 times in a row, noting that the capture process was influenced by multiple factors, yielding an overall success rate of ≈66.7% (Figures S1 and S2, Supporting Information). Figure 1f demonstrates a similar process for capturing a moving Paramecium between t = 0.28 and 0.75 s, with release occurring at t = 16.37 s. Additionally, the biocompatibility and the safety of interactions have been discussed in Figures S45 and S3 (Supporting Information). The capture and release of fast-moving objects are facilitated by the significant, rapid-response deformations enabled by our novel integration strategy, which involves thin, high-performance microactuators self-rolled around a fiber taper. Furthermore, microactuators with various configurations can also be integrated onto optical fibers through self-rolling, enabling specialized functions such as mechanical stimulation at the single-cell level. The proposed waveguide microactuators can additionally be integrated with catheters, thus facilitating operation in unstructured, enclosed environments where actuation by free-space illumination is impractical. Our waveguide microactuators and integration strategy therefore provide a high-performance solution for actuator-fiber integration, surpassing existing waveguide actuators in actuation speed, bending amplitude, and flexibility of structural design (see Table S1, Supporting Information), and paving the way for biomedical applications in constrained environments.

2. Results

2.1. Design of the poly(N-isopropylacrylamide)/Au Bilayer Heterostructure

To create a waveguide microactuator with a large bending amplitude and fast response, we designed a bilayer heterostructure consisting of an Au thin film and a poly(N-isopropylacrylamide) (pNIPAM) hydrogel layer (see Experimental Section; Figure S4, Supporting Information, for fabrication details). In this configuration, pNIPAM hydrogel can produce in-plane isotropic expansion and contraction with temperature changes. The ultra-thin Au film (≈5 nm thick), which can barely stretch or compress, restricts in-plane deformation of the hydrogel and transforms it into out-of-plane bending. Upon temperature variation, the pNIPAM hydrogel undergoes a hydrophilic-to-hydrophobic transition, which changes its shape with linear swelling ratio from 1.23 to 0.88 between 20 to 40 °C, which is equals to a strain from 23% to −12%. (Figure S5, Supporting Information). As illustrated in **Figure 2a**, when the temperature is below the lower critical solution temperature (T<LCST≈29 °C), the hydrogel is in a hydrophilic state where water molecules migrate from the external environment into the gel network, resulting in an increase in the hydrogel's volume.[28] When the hydrogel is heated to T>LCST, it transits to a hydrophobic state, resulting in the diffusion of water molecules from the gel network to the external environment and a reduction in its volume. The increase and decrease of the hydrogel's volume lead to the bending of the heterostructure
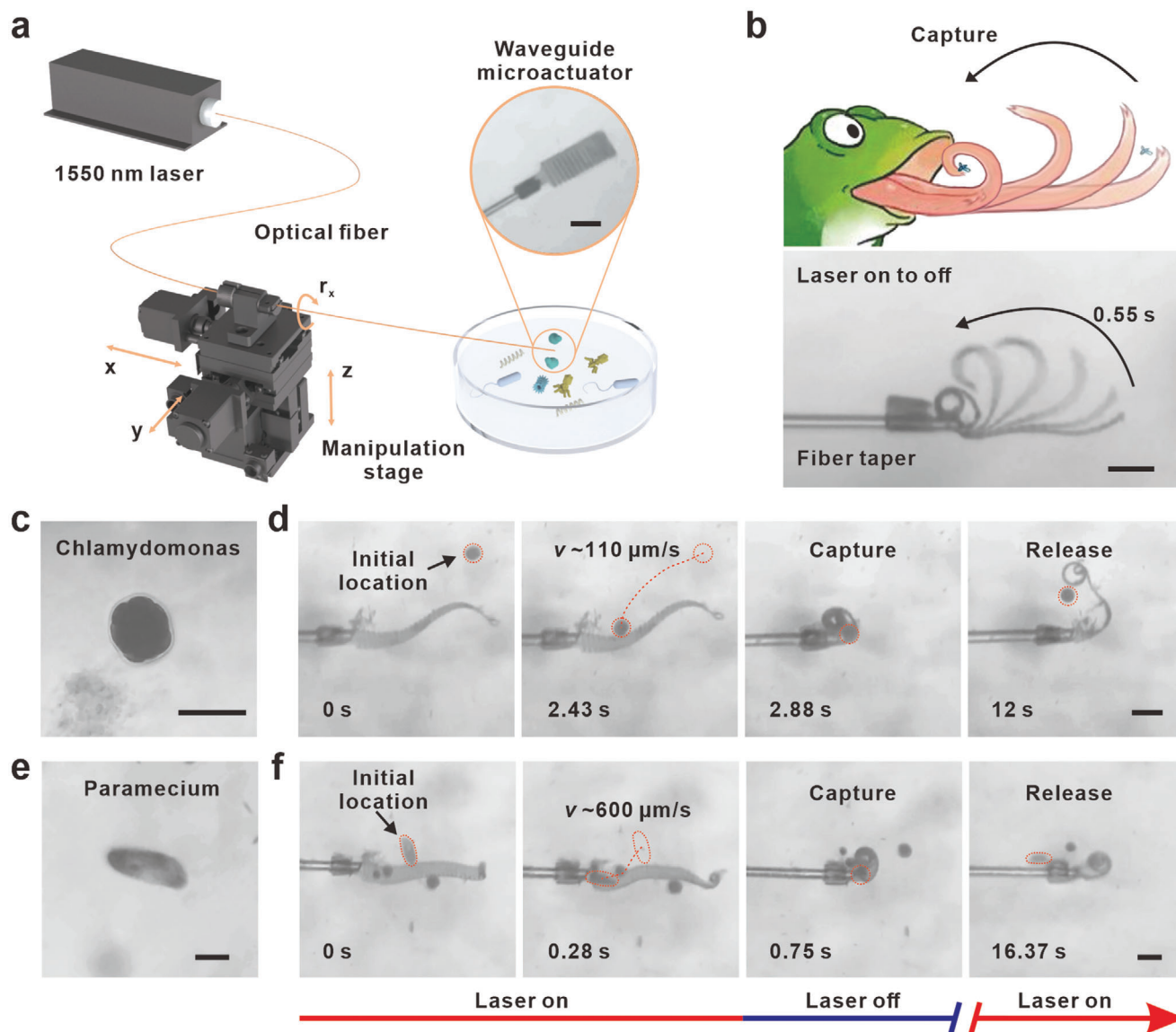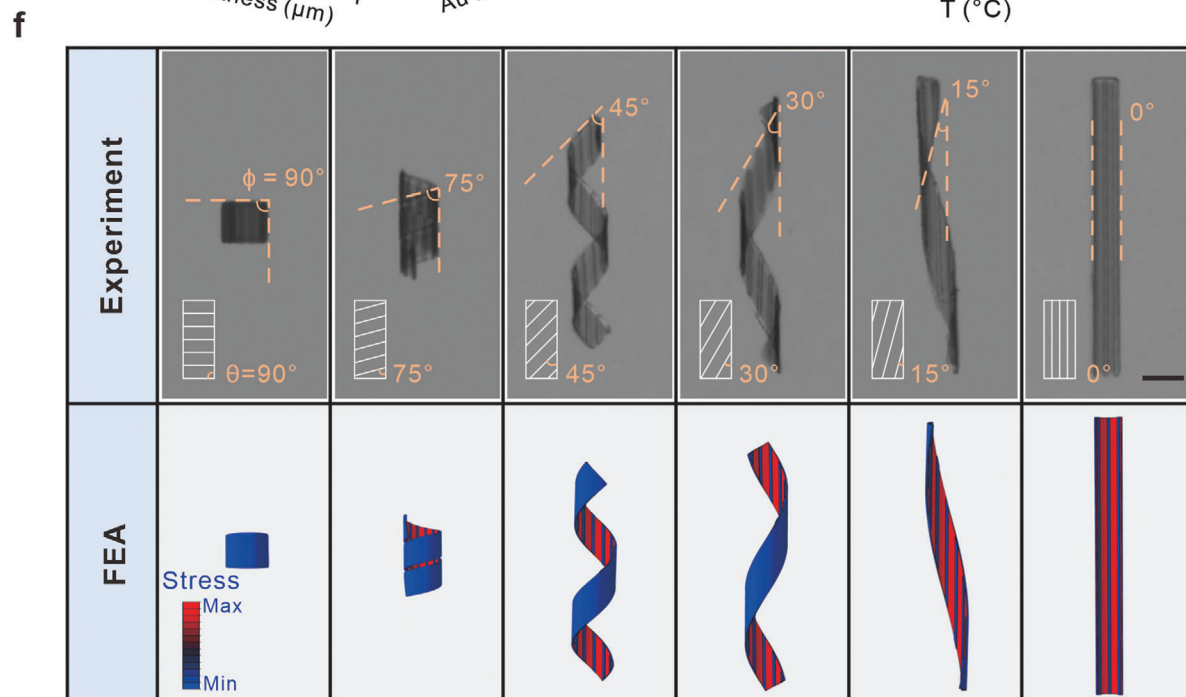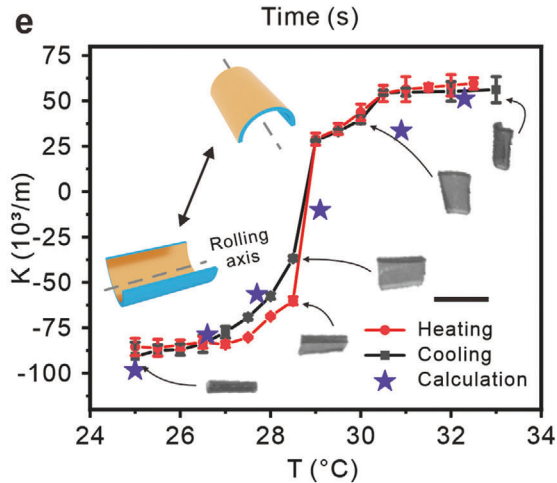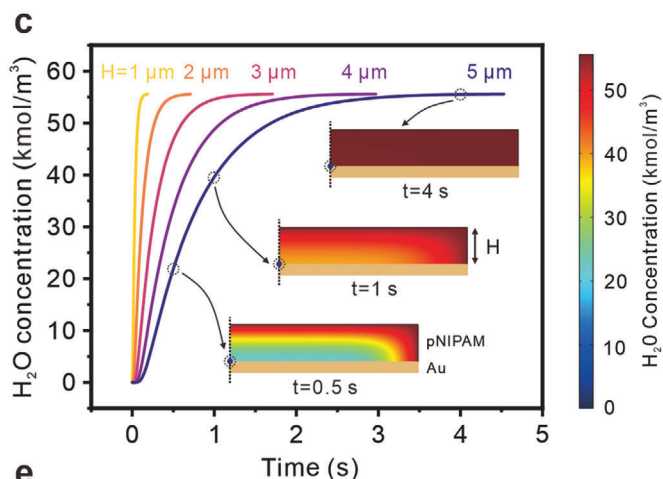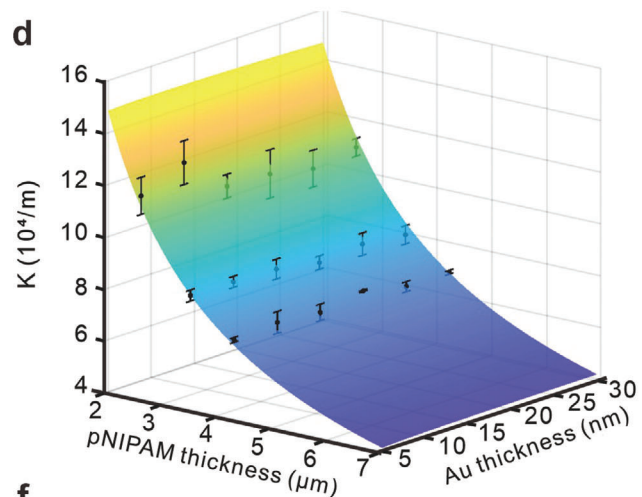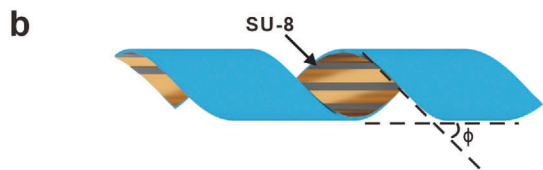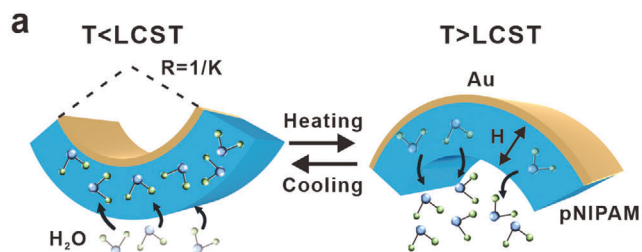
Figure 1. Setup and actuation of the waveguide microactuators and capture of fast-moving microorganisms. a) Schematic of the setup of the waveguide microactuator. Inset, optical microscope image of a fully extended microactuator. Scale bar, 100 μm. b) Schematic of the actuation of a frog's tongue and optical image of a waveguide microactuator. Scale bar, 75 μm. c,e) Optical images of a Chlamydomonas and a Paramecium, respectively. Scale bar, 50 μm. d,f) Capture and release of moving Chlamydomonas and Paramecium with the waveguide microactuator. Scale bar, 75 μm.

toward or away from the Au layer side. By patterning additional rigid grid arrays made of SU-8 (see Experimental Section for fabrication details), we can further manipulate the rolling direction to create 3D helical structures, as illustrated in Figure 2b.

The deformation speed correlates with the diffusion time of water molecules, while the deformation amplitude depends on the bending stiffness of the bilayer heterostructure. We used finite element simulations to investigate the diffusion behavior of water molecules within the hydrogel network. As depicted in Figure 2c, we modeled the cross-section of the bilayer heterostructure (see Experimental Section for simulation details). In this model, water molecules diffuse into the hydrogel from its three exposed sides, while the Au layer is impermeable to water, making the midpoint of the pNIPAM/Au interface the last point

to reach equilibrium. We analyzed the time-dependent concentration of water molecules at this point for hydrogels with thicknesses H = 1 to 5 μm. As the thickness of the hydrogel increases, the time required to reach equilibrium also increases, ranging from 0.19 s at H = 1 μm to 4.53 s at H = 5 μm, indicating that thicker hydrogels require longer to completely swell. Therefore, a thinner hydrogel results in a shorter swelling time, corresponding to a faster deformation speed.

Further, we examined the bending curvature as the deformation amplitude when a 20% strain is generated in the hydrogel. Bilayer heterostructures with various thickness combinations of pNIPAM (2.6–4.3 μm) and Au (5–30 nm) layer are fabricated and tested for their curvature below the LCST at T = 20 °C, as shown in Figure 2d, and above LCST at T = 40 °C (Figure S6,

**ADVANCED
SCIENCE NEWS**

www.advancedsciencenews.com

**ADVANCED
MATERIALS**

www.advmat.de

Supporting Information). The curvature predicted by the bending theory of elastic plates (Note S1, Supporting Information) agrees well with the experimental results. Both theory and experiment indicate that the curvature of the bilayer structure increases as the thickness of both the Au and pNIPAM layers decrease. Therefore, thinner Au and pNIPAM layers facilitate greater curvature, resulting in a larger deformation amplitude.

Two different types of deformations, single-directional bending, and cross-ply bending, are observed upon temperature variation in various thickness combinations of the two layers (Figure S7, Supporting Information), which is similar to the previous research.[29,30] In single-directional bending, the rolling axis of the structure remains unchanged during the swell and shrink of the hydrogel, while in cross-ply bending, the rolling axis switches to the perpendicular direction. For a 100 μm square bilayer structure pNIPAM (2.6 μm thick)/Au (5 nm thick) that demonstrates cross-ply bending (Figure 2e), the structure rolls up as a microtube with diameter of ≈20 μm when at T = 25 °C below the LCST. As the temperature gradually rises, the hydrogel layer shrinks, and the microtube gradually unfolds and then rolls up along the perpendicular direction until around T = 32 °C (above the LCST), with the diameter stabilizing at ≈35 μm. A similar but reversed behavior is observed during the cooling process. The microtube undergoes a large curvature change from ≈-9×10^4 to ≈5.5×10^4 m^{-1}, which agrees well with the calculation based on the bending theory of elastic plate (Note S1, Supporting Information).

The rolling direction can be controlled by patterning arrays of rigid strips with a specific orientation on top of the bilayer structures. The rigid strips here are made by 5 μm-wide SU-8 patterned by optical lithography (see Experimental Section for detailed fabrication). As shown in Figure 2f, the bilayer structure rolls parallel to the strip arrays, so that the helix angle ϕ is always equal to the orientation θ of the rigid strips. The finite element simulations also show that the SU-8 rigid strips guide the rolling of the bilayer structures, in good agreement with the experiments. Therefore, by adjusting the orientation θ of the patterned strips, bilayer structures can roll in any desired direction. In addition, by changing the width of SU-8 strips, the morphology of the bilayer structures can be significantly altered. As shown in Figure S8 (Supporting Information), the simulations demonstrate that as the width increases, the bilayer structure gradually transitions from a tubular shape to a folded configuration. This ability to modify structure through SU-8 width adjustment is useful for constructing more complex 3D microactuators.

2.2. Rolling the Bilayer Structure Around a Fiber Taper as the Waveguide Microactuator

We designed and fabricated a T-shaped structure (3.5 μm thick pNIPAM, 5 nm thick Au, and 2 μm thick SU-8, see Figure S9,

Supporting Information and Experimental Section) which self-rolled around an optical fiber taper as shown in **Figure 3a**. The upper part of the T-shaped structure serves as the winding connection, which binds to fiber taper when released from the substrate, while the lower part functions as the microactuator, which is freely actuated by the laser. The fiber taper is created through flame-heated taper drawing from standard optical fibers (see Figure S10, Supporting Information). This process produces a tapered region ≈1.5–2 mm long, ending in a tip with a diameter of ≈20–40 μm. The tip size closely matches that of the microactuator, enabling the actuator to smoothly self-roll onto the fiber, which is achievable with standard fibers (see Figure S11, Supporting Information). 1550 nm laser can be transmitted over long distances with low loss through optical fibers, enabling in efficient heat generation by the laser for photothermal actuation emitting from the fiber tip. The simulations of light propagating within the microactuators are shown in Figure S12 (Supporting Information). The laser emitted from the tip of the optical fiber illuminates the actuator in bending and straight state. The light beam can smoothly enter the actuator and undergo refraction due to the influence of the actuator, indicating that the proposed waveguide microactuator can effectively interact with the laser emitted from the optical fiber. As shown in Figure 3a and Movie S4 (Supporting Information), the fiber taper is aligned with the winding connection using a micromanipulator. After introducing water to dissolve the polyvinyl alcohol (PVA) sacrificial layer, the T-shaped structure is released from the substrate. The pNIPAM hydrogel swells after absorbing the water, so that the winding connection rolls up around the fiber taper along with the rolling of the microactuator. The microactuator in front of the fiber taper is illuminated by the laser, which heats up and unfolds. The winding connection, located behind the taper, is not sufficiently illuminated and heated, so it maintains its shape and acts as a stable connection. By switching the laser between on and off, the microactuator undergoes reversible unfolding and rolling. This deformation is quantified by the extension of the microactuator as the actuation distance L, as shown in Figure 3a.

The deformation amplitude and speed of the microactuator can be dynamically controlled by laser power. As the power increases from 0 to 10.6 mW quasi-statically, a 300 μm-long microactuator gradually unfolds and extends, as shown in Figure 3b when environment temperature is at 26.5 °C. When the laser is off at 0 mW, the microactuator fully rolls up. For laser powers below 8 mW, the maximum actuation distance increases with increasing power. When the power reaches 10.6 mW, the actuation distance initially reaches a peak (actuator fully extended), but then gradually decreases and stabilizes at an equilibrium value. This phenomenon occurs because when the power is too high, the hydrogel layer expands further, resulting in downward bending of the bilayer heterostructure with a decrease in the equilibrium actuation distance. Similar phenomena are observed when

Figure 2. Design of the pNIPAM/Au bilayer heterostructures. a) Schematic of deformation of pNIPAM/Au bilayer heterostructures induced by diffusion of H$_2$O molecules. b) Schematic of rolling direction control by a SU-8 strips array. c) The equilibrium diffusion time of H$_2$O molecules in pNIPAM layers in different thicknesses. d) Experiment and calculation results for the curvature of the bilayer heterostructures with Au and pNIPAM hydrogel layers in different thicknesses. e) Experiment and calculation results for the curvature of the bilayer at different temperatures during heating and cooling. Scale bar, 100 μm. f) Experiment and simulation results of the rolled-up bilayer with orientation θ = 90°, 75°, 45°, 30°, 15° and 0° and their corresponding helix angle ϕ. Orientation θ is defined by the angle between the stripes and the long side of rectangle. Helix angle ϕ is define by the angle between the rolling axis and the helical line. Scale bar, 50 μm.
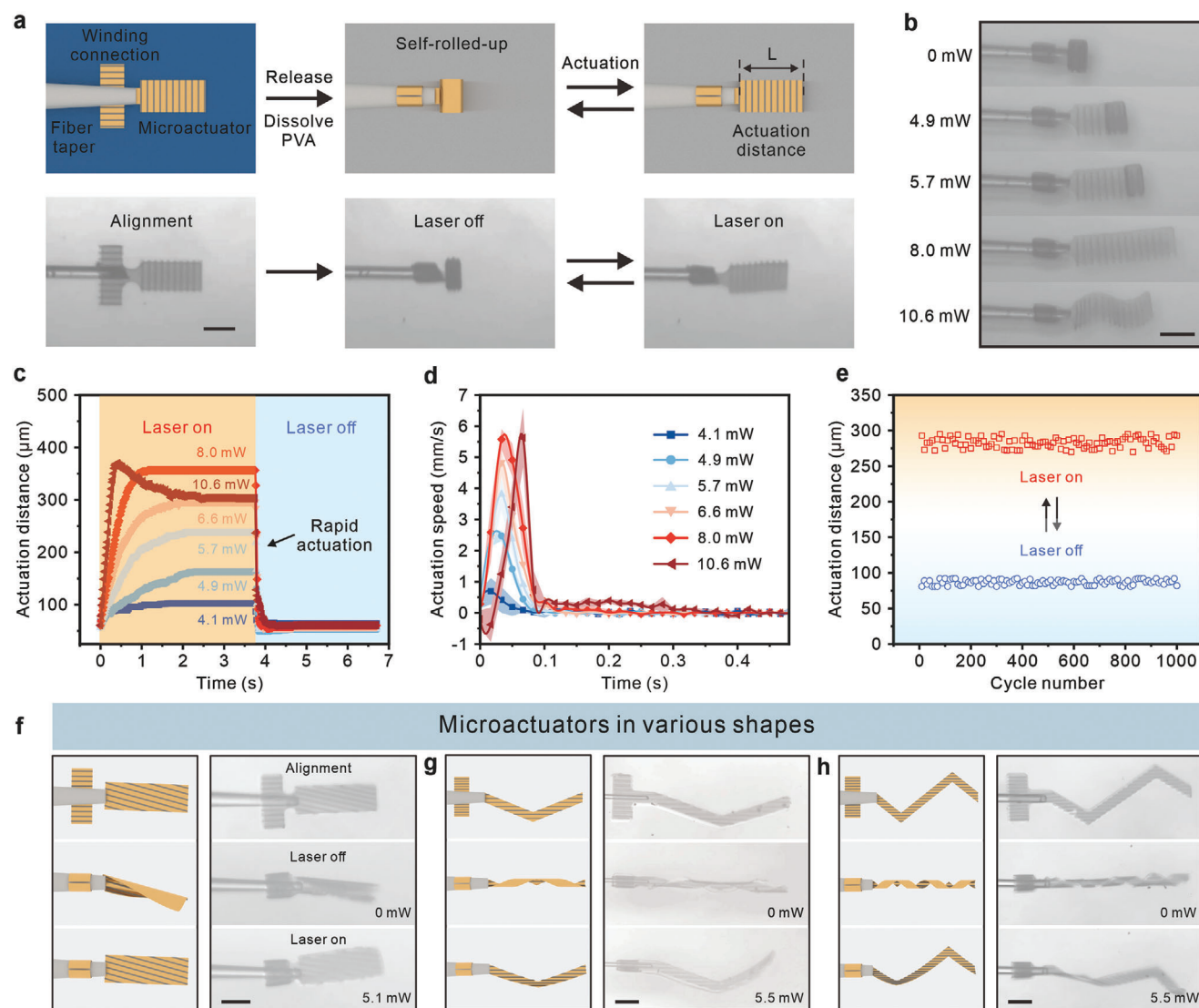
Figure 3. Fabrication and actuation of the waveguide microactuators. a) Schematic and optical images of the waveguide microactuators during fabrication and actuation. Scale bar, 100 µm. b) Optical images of a waveguide microactuator actuated by in different laser powers. Scale bar, 100 µm. c,d) Actuation distance L and Actuation speed v of the waveguide microactuators actuated in different laser powers, and the shaded regions in (d) indicate the standard deviation. e) Actuation distance of the waveguide microactuators under 1000 cycles actuation with 7.1 mW laser power. f-h) Schematic and optical images of the microactuators in various shapes showing distinct actuation behaviors. Scale bars, 75 µm.

we measured the actuation distance over time at different laser powers, as shown in Figure 3c; Figure S13 and Movie S5 (Supporting Information). With the laser on, it takes ≈1–3 s for the actuator to extend and the actuation distance reaches the maximum. Compared to the actuation during heating, the cooling process leads to much faster actuation. When the laser is off, it takes ≈0.3–0.7 s for the actuator to fully roll-up (see Figure S14, Supporting Information), and the actuation distances returns to minimum. We measured the actuation speed during cooling when laser is turned off at various laser powers. As illustrated in Figure 3d, the actuation speed reached its peak within 0.1 s with the maximum speed up to 6 mm s^{-1} when irradiated by 8.0 or 10.6 mW laser. Subsequently, the actuation speed rapidly declined and eventually converged to zero between 0.1 s to 0.5 s. We note that in the case of 10.6 mW, the actuation speed

decreases during the initial 0.01 s. This is because the microactuator undergoes a process from bending downward to flattening, causing a negative actuation speed. Further explanations can be found in Figure S15 (Supporting Information). This figure also shows that the maximum actuation speed increases along with the increased laser power. This is because as the laser power increases, higher photothermal conversion occurs, which leads to an increased temperature difference between the actuator and the medium. Upon turning off the laser, a larger temperature difference between the microactuator and environment results in a greater heat dissipation rate (see Note S2, Supporting Information). A similar trend is observed when laser is turned on (Figure S16, Supporting Information). It is worth mentioning that deformation is also affected by the environment temperature, which modifies the strain in the hydrogel layer during the heating and

**ADVANCED
SCIENCE NEWS**

www.advancedsciencenews.com

**ADVANCED
MATERIALS**

www.advmat.de

cooling cycle. The complex actuation behaviors at various environment temperature are studied in Figures S17–S21, Movie S6, and Note S2 (Supporting Information). Finally, we conducted a study on the stability of repeated deformation. As shown in Figure 3e, the waveguide microactuator exhibits minor decay in performance after more than 1000 actuations at 7.1 mW and at 26.5 °C. At the same time, within 1000 actuation cycles, the connection between the fiber taper and microactuator remains stable without any visible slippage or damage (Figure S22, Supporting Information). In addition, the layout of the microactuators can be tailored with various shape and grid designs, demonstrating distinct actuation behaviors. Figure 3f and Movie S7 (Supporting Information) show a ≈300 μm-long microactuator in rectangle shape that twists when actuated, whose helix angle can be controlled by the orientation θ of the rigid array similar to Figure 2f. Microactuators ≈600 μm-long with one and two kinks are shown in Figure 3g,h, respectively, which can switch between extended and helical shapes when laser is turned on and off. These distinct morphing behaviors of the microactuators may facilitate their applications in manipulating micro-objects in different shapes.

2.3. Programmable Non-Reciprocal Motion in the Waveguide Microactuators

In addition to studying the deformation amplitude and speed, we also found a non-reciprocal shape change during the heating and cooling of the waveguide microactuators, which is particularly useful for effective propulsion at the microscale in a low Reynolds number environment.[31] As shown in **Figure 4a**, the waveguide microactuators have distinct heating and cooling mechanisms when the laser is on and off. When the laser is turned on, it illuminates along a straight line, so that the bottom of the rolled-up structure heats up first and unfolds, while the rest of the structure is then heated sequentially. When the laser is turned off, the whole microactuator dissipates heat to the surrounding aqueous medium, resulting in a simultaneous cooling of the entire structure. The different heating and cooling mechanisms result in non-reciprocal tip trajectories of a 225 μm-long microactuator during the laser actuation at 5.5 mW, which is clearly observed in Figure 4b. Based on this mechanism, we established a model to simulate the non-reciprocal trajectories (Note S3, Supporting Information). The simulation results are in well agreement with the experiment, as shown in Figure 4c. The sequential heating leads to the tip motion following an upward-slanting shape similar to a cycloid, while the simultaneous cooling results in a tip trajectory resembling a Fibonacci spiral.

We define the non-reciprocal area as the area enclosed by the non-reciprocal tip trajectories, i.e., the area swept by the microactuators, which is directly proportional to the amount of liquid that can be pumped during each cycle.[32,33] We first investigated the relationship between laser power and the non-reciprocal area of a 300 μm-long microactuator. As shown in Figure 4d, the non-reciprocal area increases from 0.60×10^4 to 2.81×10^4 μm² as laser power increases from 1.2 to 7.2 mW (see Figures S23 and S24 and Movie S8, Supporting Information, for full tip trajectories). This is possibly due to the in-

creased actuation amplitude during the sequential heating and simultaneous cooling processes at higher laser power. When the laser power reaches 10.6 mW, the non-reciprocal area decreases to 1.71×10^4 μm². This may be because the expanded illumination region at the excessive laser power. Detailed discussion of this phenomenon can be referred in Note S3 (Supporting Information).

In addition, we investigated the non-reciprocal area of microactuators in different lengths, from 150 to 450 μm, at the same laser power 5.5 mW, as shown in Figure 4e. By analyzing the tip trajectories (see Figures S25 and S26 and Movie S9, Supporting Information), we found that when the microactuators are from 150 to 375 μm-long, the non-reciprocal area increases from 1.23×10^4 to 3.36×10^4 μm², due to the larger deformation result from longer microactuators. When the actuator is 450 μm-long, the part of the actuator unable to be completely heated because the excessively long length causes the this part of actuator to exceed the illuminated area, so the structure cannot fully unroll, resulting in decreased non-reciprocal area. Detailed simulations also validate the trend that the non-reciprocal area initially increases and then decreases as the microactuator length increases (Note S3, Supporting Information).

The non-reciprocal motion of the waveguide microactuator is useful for cargo transportation in low Reynolds number environment. In a proof-of-concept experiment, we placed 50 μm-diameter polystyrene (PS) microbeads in a 5 wt.% PVA solution. When a 6.4 mW laser is switched off, the microactuator folds up and pumps the microbead ≈100 μm to the left (Figure 4f). When the laser is switched on, the actuator unfolds and pumps the microbead ≈50 μm to the right (Figure 4g). Therefore, through such a non-reciprocal motion cycle, the microbead experiences a net displacement of ≈50 μm to the left. We also tested the displacement of a microbead over multiple actuation cycles, confirming that similar net displacements were generated in each cycle (see Figure 4h; Movie S10 and Figure S27, Supporting Information). This pumping action is also useful for manipulating objects much smaller than the microactuator, which are difficult to hook or grasp directly. We tracked the movement of suspended yeast cells, ≈5 μm in diameter, at three different positions in the liquid (Figure 4i), demonstrating that the waveguide microactuator can effectively pump yeast cells toward left, as shown in Figure 4j and Movie S11 (Supporting Information). Figure 4k shows the displacement of a tracked yeast cell along the x-axis over multiple actuations.

3. Discussion

In summary, we developed waveguide microactuators based on a micropatterned pNIPAM /Au bilayer heterostructure self-rolled around an optical fiber taper. The microactuators feature in large bending angles (>800°) with fast responses (≈0.55 s), enabling the effective capture of fast-swimming microorganisms. This capability arises from a thin hydrogel layer that quickly absorbs and releases water molecules in a hydrophilic-to-hydrophobic phase transition, facilitating swift deformation of the microactuators. The self-rolled-up integration method allows the microactuator to be accurately and stably bonded to a fiber taper, while the microactuator can be designed in various shape with tailored morphing behaviors. Furthermore, because
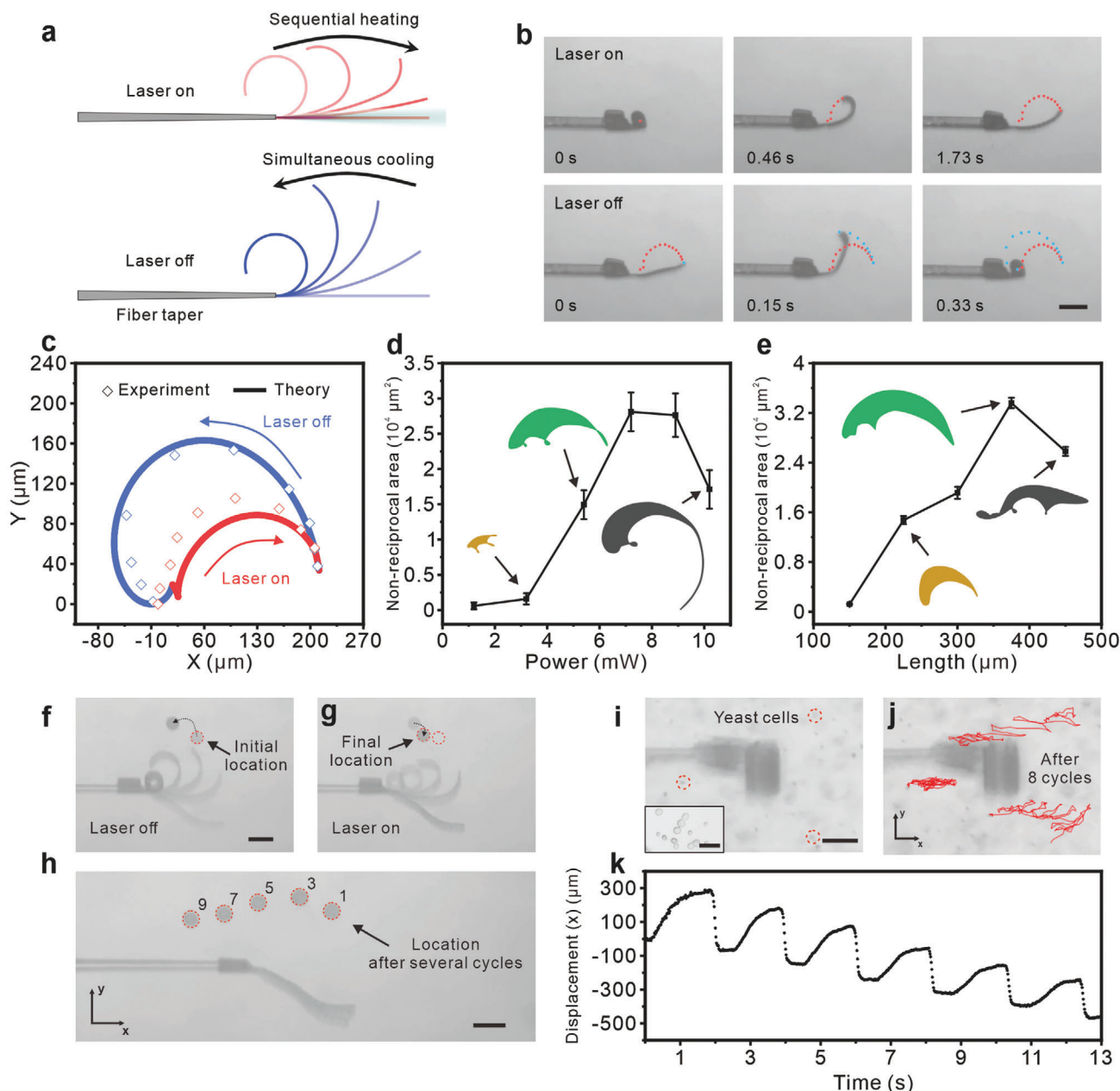
**ADVANCED
SCIENCE NEWS**

www.advancedsciencenews.com

**ADVANCED
MATERIALS**

www.advmat.de

Figure 4. Non-reciprocal motion of the waveguide microactuators and their applications for non-contact pumping. a) Schematic of the heating and cooling mechanisms during laser on and off resulting in non-reciprocal motion of the microactuator. b) Optical images of a 225 μm-long microactuator with tip trajectories when the laser is turned on (upper) and turned off (down) at 5.5 mW. Scale bar, 100 μm. c) Tip trajectories of the waveguide microactuator from experiment results and theoretical calculations actuated by a 5.5 mW laser. d) Measured non-reciprocal area for the 300 μm-long microactuator actuated by different laser power. e) Measured non-reciprocal area for microactuators actuated by a 5.5 mW laser. f,g) Time-lapse optical image for the deformation of the microactuator and the corresponding movement of the PS microbead, when laser is turned off and turn on, respectively. Arrow represents the direction of the movement. Scale bar, 75 μm. h) Optical image illustrating locations of the PS microbead after several pumping cycles of the microactuator. Scale bar, 75 μm. i) Optical image for the waveguide microactuator and the yeast cells before pumping. The dotted circles highlights the location of the tracked yeast cells. Scale bar, 75 μm. Inset, optical image of yeast cells. Scale bar, 10 μm. j) Optical image illustrating trajectories of the yeast cells after 8 pumping cycles. k) Displacement of the yeast cells along x-axis during pumping cycles.

of the intrinsically distinct heating and cooling mechanisms for a microactuator in front of a fiber taper, the microactuators demonstrate non-reciprocal shape morphing which can be easily programmed by laser power. This non-reciprocal motion is implemented for pumping microbeads and yeast cells, providing flexi-

ble and non-contact manipulation of objects that are challenging to directly capture at the microscale.

Thanks to the microfabrication techniques we used, our waveguide microactuators may be customized within a large variety of shapes, according to the shape and size of the

**ADVANCED
SCIENCE NEWS**

www.advancedsciencenews.com

**ADVANCED
MATERIALS**

www.advmat.de

micro-object to be manipulated in applications. Cell squeezer, a foldable waveguide microactuator that can apply mechanical stimuli to isolated cells, has been developed to demonstrate potential applications in single-cell level biomedical research (see Note S4 and Movie S12, Supporting Information). We conducted proof-of-concept experiment to demonstrate the possibility of integrating our waveguide microactuators with catheters (see Figure S46, Note S5, and Movie S13, Supporting Information). The waveguide microactuator nested in the tube navigated through curved microchannels and achieved stable actuation within an enclosed chamber, which demonstrating its application potential in unstructured and confined working environments. To achieve even faster deformation, pNIPAM/Au nanocomposite hydrogel with high photothermal conversion efficiency[26] may replace the the hydrogel used in this work. We note that high laser power (e.g., 10.6 mW) can induce excessive heating, causing the pNIPAM hydrogel to shrink. This shrinkage leads to negative strain and prompts the bilayer structure to bend downward. Such behavior results in an increased response time (see Figure S14, Supporting Information) and a reduced non-reciprocal area, which lowers pumping efficiency (see Figure 4d). To mitigate these effects, increasing the LCST of the hydrogel, such as by grafting hydrophilic monomers like acrylic acid onto pNIPAM, could allow the material to retain a positive strain at higher temperatures.[34] This adjustment would extend the temperature (and thus laser power) range over which the bilayer maintains optimal performance, preventing downward bending and its associated drawbacks. In the future, the waveguide microactuators may be further integrated with nanosensors such as nanoparticles and molecular probes for sensing,[35,36,37] or loaded with drug molecules for treatment,[38] thereby achieving a multi-functional fiber-based intelligent platform for in situ cell research. This technique may have wide applications in enclosed environments where free-space illumination is not possible.

4. Experimental Section

poly(N-isopropylacrylamide) Synthesis: Poly(N-isopropylacrylamide-co-4-Benzoylphenyl acrylate) was synthesized by free radical polymerization with azobisisobutyronitrile (AIBN) as initiator. This process was adapted from previous research.[39] N-isopropylacrylamide (1.00 g, Aladdin), 4-Benzoylphenyl acrylate (0.02253 g, Aladdin), and AIBN (0.01453 g, Aladdin) were dissolved in 6 mL of 1,4-dioxane. The reaction was conducted under 80 °C for 24 h after a nitrogen purge for 30 min. The generated polymer was precipitated in diethyl ether to remove the small molecule, and then suction filtered. Filtered products were finally dried in a vacuum oven for 24 h. AIBN was purified by recrystallization. All other chemicals were used as received. The synthesized pNIPAM hydrogel was confirmed by FTIR and NMR, which can be shown in Figures S28 and S29 (Supporting Information). According to the results of GPC (Figure S30, Supporting Information), the M_n of synthesized pNIPAM was 48 466 Da, while polydispersity was ≈1.460.

Fabrication of poly(N-isopropylacrylamide)/Au Bilayer Heterostructures, Waveguide Microactuators and Optical Fiber Tapers: Silicon wafers were cut into 1.5 cm × 1.5 cm pieces and pre-cleaned by ultrasonic cleaning with acetone, ethanol, and water for 15 min, and then dried with a nitrogen gun. The cleaned substrates were treated by oxygen plasma for 3 min before spin coating. After all these treatments, Polyvinyl alcohol (degree of Hydrolysis 87%–89%, 5 wt.% aqueous solution) sacrificial layer was spin-coated on the substrate with 600 rpm for 6 s and 2000 rpm for 90 s. After

evaporating the residual solvent on a 110 °C hot plate, pNIPAM copolymer solution (0.1 mg pNIPAM dissolved in mixed solvents with 1 mL isopropanol and 0.5 mL chloroform, thickness of the pNIPAM film by spin-coating can be found in Figure S31, Supporting Information) was spin-coated with 600 rpm for 6 s and 1500 rpm for 30 s, and then heated for 30 s on 100 °C hot plate. After spin-coating process, the substrate was covered by a shadow mask with desired patterned pores (rectangle or T-shaped). Similar processes using templating[25] may also be used to patterning. and exposed under the 0.9 mW cm^{-2} 275 nm UV light for 60 s. Afterward, 5 nm Au film was deposited on the substrate covered by shadow mask. Then the shadow mask was peeled off from the substrate, and the substrate was immersed in the chloroform for 60 s to dissolve uncrosslinked portions of the film to obtain the patterned pNIPAM/Au bilayer heterostructures. The SU-8 (SU-8 2002.5 photoresist) strips that control the rolling direction and thick SU-8 layer (SU-8 2015 photoresist) used in cell squeezers were fabricated on pNIPAM/Au bilayer heterostructures using conventional UV lithography (SUSS, MA6). Finally, the substrate was immersed in an aqueous medium to dissolve the sacrificial layer and release the structures. Optical fiber tapers were taper-drawn from standard optical fiber (SMF-28E,125 μm) by using a homemade fiber-tapering system. A fire-brush system was designed to extend the waist length by allowing the motors to stretch the fiber in opposite directions while moving together. By adjusting the stretching program, fiber tapers with controllable diameters were produced.

Characterization and Measurements: The morphology of pNIPAM/Au bilayer heterostructures, waveguide microactuators, and optical fiber tapers was characterized by optical microscope (Zessis, Axiolab5). The absorbance spectrum of pNIPAM was measured using a FTIR spectrophotometer (Bruker, Vertex70). The thickness of films was tested by Profilometry (Bruker, Dektak XT). All temperature control experiments were achieved through real-time calibration of digital heat stage and thermocouples. The actuation behaviors of pNIPAM/Au bilayer heterostructures and waveguide microactuators were captured by a CCD camera integrated on the optical microscope. The analysis of deformation trajectory was completed by the image tracking software Tracker. The light source for all actuation experiment of waveguide microactuators was a 1550 nm Laser (MW-GX-1550). The laser power emitted from the optical optic was calibrated by an optical power meter (THORLABS, PM100D). The optical fibers were controlled using assembled mechanical threaded micromanipulation platforms. Curved microchannel was been fabricated by computer numerical control (CNC) micromachining, and stacked with another glass slide to form an enclosed microchannel. Flexible tubes were purchased in rubber products store online. The FTIR was conducted by Bruker Vertex 70. The NMR was conducted by Bruker Avance 400. The GPC was conducted by PL-GPC50. The vis–IR spectrum was tested by Jasco V-770.

Culture of Microorganisms and Yeast Cells: Paramecium and Chlamydomonas were purchased directly from microbial aquarium and cultured in specially culture medium (0.25 g NaHCO$_3$, 0.2 g glucose in 1L RO water) to maintain vitality at 26 °C. Here we used Parameciumbursaria that were 100–200 μm in length, which was smaller than standard Paramecium. The Chlamydomonas used were ≈30–50 μm in diameter. During the experiment, Paramecium and Chlamydomonas were directly aspirated and dropped onto the substrate from the pre-shaken culture medium. For yeast cells, the corresponding liquid culture medium (a mixed solution of glucose and water) was prepared first, then added dry yeast, and stored it in a constant temperature box at 26 °C for 36 h to allow the yeast to fully reproduce. Finally, we obtained yeast cells with size of ≈3–5 μm. During the experiment, we diluted the yeast solution to an appropriate concentration and then shaken and dropped the yeast solution onto the substrate for the experiment.

FEA Simulations: The commercial finite-element analysis software ABAQUS and COMSOL Multiphysics were used for the deformation configuration analysis of pNIPAM/Au bilayer heterostructures (Figure 2f), water molecular diffusion model (Figure 2c) in hydrogel, and square of electric field mode $|E|^2$ distribution of emitted laser from optical fiber taper (Figure S12 and S34, Supporting Information). In ABAQUS, the response of the pNIPAM in temperature was introduced as a volumetric stress. The

**ADVANCED
SCIENCE NEWS**

www.advancedsciencenews.com

**ADVANCED
MATERIALS**

www.advmat.de

deformation configuration of pNIPAM/Au bilayer heterostructures was investigated with SU-8 strips in different directions under a predefined field of volumetric stress of 540 000 Pa, which was ≈0.07 strain of pNIPAM. For the simulations of different width of SU-8 strips, a predefined field of volumetric stress was set as 260 000 Pa. For the simulations of the cell compression of cell squeezer, a predefined field of volumetric stress was set as 280 000 Pa. The thicknesses of Au (Young's modulus 70 GPa, Poisson's ratio 0.42) layer, pNIPAM (Young's modulus 8 MPa, Poisson's ratio 0.3) layer, and SU-8 (Young's modulus 4.6 GPa, Poisson's ratio 0.252) layer were 5 nm and 2.5 and 2.5 μm/20 μm (in simulations of the cell compression of cell squeezer), respectively. The elastic modulus and Poisson's ratio of the cell were set to 20 kPa and 0.3. Geometrical nonlinearities were accounted for during the simulation. In COMSOL Multiphysics, the transient study of dilute matter transport was used to study the diffusion of water molecules in hydrogel. Here, according to the data in the reference,[40] the diffusion coefficient of water molecules in gel was set to 1.5×10^{-11} m^2 s^{-1}. The three edges of the hydrogel (two wide edges and one long edge) were set as inflow boundary conditions. A long side was set as the symmetry condition (water molecules could not enter from this boundary). The grid was divided into free triangular grids. In COMSOL Multiphysics, wave optics module with beam envelope method was used to simulated the electric field mode distribution of emitted laser from optical fiber taper. This study assumed that the inner cores and outer cores of standard optical fibers were proportionally reduced during the drawing process. The diameters of the inner and outer cores of optical fiber taper were set to 8.2 and 125 μm, which were linearly reduced along the length (cone length: 2 mm) to 1.312 and 20 μm. The refractive index of the inner and outer cores of the optical fiber remains unchanged, which were set to 1.4457 and 1.4378, respectively. The real part of the refractive index of water was set to 1.33, and the imaginary part was set to 9.73×10^{-6}. The refractive index of the pNIPAM hydrogel was set to 1.433. The surface of the optical fiber was equipped with a 1 μm Perfectly Matched Layer. The input optical power of the port was set to 10 mW.

4T1 Cells and Cytotoxicity Evaluation: The cell squeezer on the slides was sterilized by ultraviolet irradiation and cocultured with mouse breast cancer cells (4T1 cells, purchased from the Cell Bank/Stem Cell Bank of the Chinese Academy of Sciences; cultured in 1640 complete medium containing 10% Fetal bovine serum (FBS) and 1% Penicillin-Streptomycin) for 18, 24, 36, and 48 h, respectively, in a constant temperature incubator (37 °C, 5% CO$_2$). The cultured cells were stained by Calcein acetoxymehtyl ester / Propidium iodide (Calcein-AM/PI) double-stain kit and incubated at room temperature for 30 min. Fluorescence microscope (Leica DMi8) was used to obtain the images of dyed live and dead cells. The RPMI 1640 medium, dual antibiotics (Penicillin-Streptomycin), Calcein-AM, and PI were purchased from Adama's life. FBS was purchased from Gibco.

Supporting Information

Supporting Information is available from the Wiley Online Library or from the author.

Conflict of Interest

The authors declare no conflict of interest.

Data Availability Statement

The data that support the findings of this study are available from the corresponding author upon reasonable request.

[1] J. Shintake, V. Cacucciolo, D. Floreano, H. Shea, *Adv. Mater.* **2018**, *30*, 1707035.

[2] L. Zhou, L. Ren, Y. Chen, S. Niu, Z. Han, L. Ren, *Adv. Sci.* **2021**, *8*, 2002017.

[3] E. Acome, S. K. Mitchell, T. G. Morrissey, M. B. Emmett, C. Benjamin, M. King, M. Radakovitz, C. Keplinger, *Science* **2018**, *359*, 61.

[4] C. Wang, K. Sim, J. Chen, H. Kim, Z. Rao, Y. Li, W. Chen, J. Song, R. Verduzco, C. Yu, *Adv. Mater.* **2018**, *30*, 1706695.

[5] Z. Liu, H. K. Bisoyi, Y. Huang, M. Wang, H. Yang, Q. Li, *Angew. Chem., Int. Ed.* **2022**, *61*, 202115755.

[6] X. Yang, L. Lan, X. Pan, Q. Di, X. Liu, L. Li, P. Naumov, H. Zhang, *Nat. Commun.* **2023**, *14*, 2287.

[7] X. Pang, J.-a. Lv, C. Zhu, L. Qin, Y. Yu, *Adv. Mater.* **2019**, *31*, 1904224.

[8] C. Xin, Z. Ren, L. Zhang, L. Yang, D. Wang, Y. Hu, J. Li, J. Chu, L. Zhang, D. Wu, *Nat. Commun.* **2023**, *14*, 4273.

[9] G. Cai, J.-H. Ciou, Y. Liu, Y. Jiang, P. S. Lee, *Sci. Adv.* **2019**, *5*, eaaw7956.

[10] Y. Tang, M. Li, T. Wang, X. Dong, W. Hu, M. Sitti, *Adv. Mater.* **2022**, *34*, 2204185.

[11] H.-W. Huang, M. S. Sakar, A. J. Petruska, S. Pané, B. J. Nelson, *Nat. Commun.* **2016**, *7*, 12263.

[12] G. Gu, J. Zou, R. Zhao, X. Zhao, X. Zhu, *Sci. Rob.* **2018**, *3*, eaat2874.

[13] X. Li, J. Liu, D. Li, S. Huang, K. Huang, X. Zhang, *Adv. Sci.* **2021**, *8*, 2101295.

[14] J. Li, X. Zhou, Z. Liu, *Adv. Opt. Mater.* **2020**, *8*, 2000886.

[15] Y. Li, Y. Liu, D. Luo, *Adv. Opt. Mater.* **2021**, *9*, 2001861.

[16] M. Zhang, A. Pal, X. Lyu, Y. Wu, M. Sitti, *Nat. Mater.* **2024**, *23*, 560.

[17] Y. Zhao, C. Xuan, X. Qian, Y. Alsaid, M. Hua, L. Jin, X. He, *Sci. Rob.* **2019**, *4*, eaax7112.

[18] M. Pilz da Cunha, H. S. Kandail, J. M. J. den Toonder, A. P. H. J. Schenning, *Proc. Natl. Acad. Sci. U.S.A.* **2020**, *117*, 17571.

[19] H. Shahsavan, A. Aghakhani, H. Zeng, Y. Guo, Z. S. Davidson, A. Priimagi, M. Sitti, *Proc. Natl. Acad. Sci. U.S.A.* **2020**, *117*, 5125.

[20] Y. Zhang, J. Zheng, F. Jin, J. Xiao, N. Lan, Z. Xu, X. Yue, Z. Li, C. Li, D. Cao, Y. Wang, W. Zhong, Y. Ran, B.-O. Guan, *Light: Sci. Appl.* **2024**, *13*, 228.

[21] A. S. Kuenstler, H. Kim, R. C. Hayward, *Adv. Mater.* **2019**, *31*, 1901216.

[22] J. Xiao, T. Zhou, N. Yao, S. Ma, C. Pan, P. Wang, H. Fu, H. Liu, J. Pan, L. Yu, S. Wang, W. Yang, L. Tong, L. Zhang, *Nat. Commun.* **2022**, *13*, 363.

[23] Y. Zhou, A. W. Hauser, N. P. Bende, M. G. Kuzyk, R. C. Hayward, *Adv. Funct. Mater.* **2016**, *26*, 5447.

[24] M. Zmyślony, K. Dradrach, J. Haberko, P. Nałęcz-Jawecki, M. Rogóż, P. Wasylczyk, *Adv. Mater.* **2020**, *32*, 2002779.

[25] A. Mourran, H. Zhang, R. Vinokur, M. Möller, *Adv. Mater.* **2017**, *29*, 1604825.

[26] H. Zhang, A. Mourran, M. Möller, *Nano Lett.* **2010**, *2017*, 17.

[27] S. Timoshenko, *J. Opt. Soc. Am.* **1925**, *11*, 233.

[28] J. Liu, L. Jiang, S. He, J. Zhang, W. Shao, *Chem. Eng. J.* **2022**, *433*, 133496.

[29] H. Wang, X. Chen, X. Meng, Y. He, B. Jin, X. Zhao, C. Ye, *Chem. Mater.* **2024**, *36*, 4174.

[30] Z. Tian, B. Xu, G. Wan, X. Han, Z. Di, Z. Chen, Y. Mei, *Nat. Commun.* **2021**, *12*, 509.

[31] E. M. Purcell, *Am. J. Phys.* **1977**, *45*, 3.

[32] S. N. Khaderi, M. G. H. M. Baltussen, P. D. Anderson, J. M. J. den Toonder, P. R. Onck, *Phys. Rev. E* **2010**, *82*, 027302.

[33] W. Wang, Q. Liu, I. Tanasijevic, M. F. Reynolds, A. J. Cortese, M. Z. Miskin, M. C. Cao, D. A. Muller, A. C. Molnar, E. Lauga, P. L. McEuen, I. Cohen, *Nature* **2022**, *605*, 681.

[34] S. J. Lue, C.-H. Chen, C.-M. Shih, *J. Macromol. Sci. Phys.* **2011**, *50*, 563.

[35] E. A. Vitol, Z. Orynbayeva, M. J. Bouchard, J. Azizkhan-Clifford, G. Friedman, Y. Gogotsi, *ACS Nano* **2009**, *3*, 3529.

[36] Y. Ran, Z. Xu, M. Chen, W. Wang, Y. Wu, J. Cai, J. Long, Z.-S. Chen, D. Zhang, B.-O. Guan, *Adv. Sci.* **2022**, *9*, 2200456.

[37] Z. Zhu, S. Sun, X. Chai, J. Gao, M. Lu, Z. Wu, Y. Gao, T. Feng, X. Bai, Y. Zhang, F. Yan, W. W. Yu, C. Ke, *Laser Photonics Rev.* **2024**, *18*, 2301388.

[38] A. Ghosh, W. Liu, L. Li, G. J. Pahapale, S. Y. Choi, L. Xu, Q. Huang, R. Zhang, Z. Zhong, F. M. Selaru, D. H. Gracias, *ACS Nano* **2022**, *16*, 16211.

[39] V. Magdanz, M. Guix, F. Hebenstreit, O. G. Schmidt, *Adv. Mater.* **2016**, *28*, 4084.

[40] J. Yoon, S. Cai, Z. Suo, R. C. Hayward, *Soft Matter* **2010**, *6*, 6004.